

# Effects of Oxygen Vacancies and Cation Valence States on the Triboelectric Property of Substoichiometric Oxide Films

Yongqiao Zhu,<sup>1</sup> Shiquan Lin,<sup>1</sup> Wenchao Gao,<sup>1</sup> Miao Zhang, Chaogui Yang, Peizhong Feng, Cheng Xu,<sup>\*</sup> and Zhong Lin Wang<sup>\*</sup>



Cite This: <https://doi.org/10.1021/acsami.1c09248>



Read Online

ACCESS |



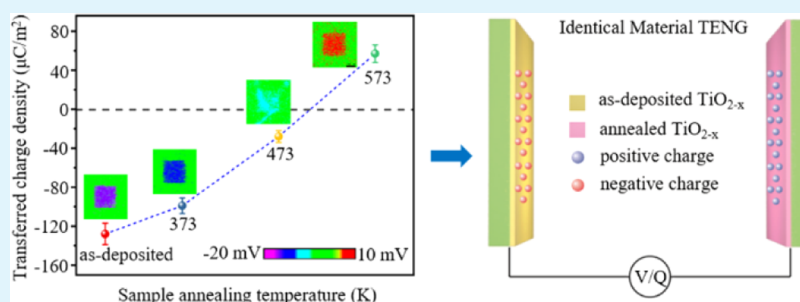
Metrics & More



Article Recommendations



Supporting Information



**ABSTRACT:** Temperature effects on the contact electrification (CE) is of great interest. Here, different kinds of substoichiometric oxide films, such as TiO<sub>2-x</sub>, Al<sub>2</sub>O<sub>3-x</sub>, Ta<sub>2</sub>O<sub>5-x</sub>, and Cr<sub>2</sub>O<sub>3-x</sub> are deposited and annealed at different temperatures, and the CE between the films and a Pt-coated tip is performed by using Kelvin probe force microscopy (KPFM). An intriguing finding is that the polarity on the TiO<sub>2-x</sub> surface changes from negative to positive with the increase of the sample annealing temperature in air atmosphere. Such a result is attributed to the fact that annealing under an oxidative atmosphere repairs oxygen vacancies and helps upgrade the low valency of Ti<sup>3+</sup> to a stable high valency of Ti<sup>4+</sup>. On the contrary, after annealing occurs in an Ar/H<sub>2</sub> atmosphere, the polarity on the TiO<sub>2-x</sub> surface reverses from positive to negative. This is mainly due to the increase of oxygen vacancies after annealing in reducing atmosphere. Through the KPFM results of Al<sub>2</sub>O<sub>3-x</sub>, Ta<sub>2</sub>O<sub>5-x</sub>, and Cr<sub>2</sub>O<sub>3-x</sub> films, the effect of oxygen vacancies is further confirmed, that is, the decrease of oxygen vacancies eases the films at capturing positive charges. Based on this, TiO<sub>2-x</sub>-based identical material triboelectric nanogenerators (IM-TENGs) are designed and prepared for the first time to control the current direction. Moreover, a surface state model for explaining the CE mechanism between the metal and annealed dielectric is proposed. This study is conducive to the development of the IM-TENGs which regulate the current direction or voltage output accurately in the future and also provides a further understanding of the dominant mechanism of electron transfer in the CE.

**KEYWORDS:** contact electrification, triboelectrification, nanogenerator, annealing, surface states

## 1. INTRODUCTION

Contact electrification (CE), one of the oldest scientific topics, was first discovered in ancient Greece about 2600 years ago. Although the CE is a common phenomenon in our daily life, the physical mechanism behind it is still unresolved and under debate.<sup>1-3</sup> As an emerging technology, the triboelectric nanogenerator (TENG) is invented based on the CE and electrostatic induction effect, which provides a new option for people to solve the world's energy problems, and the CE has also become one of the hotspots in academic community.<sup>4-9</sup>

The identity of the charge carriers is one of the core issues in the CE.<sup>10-13</sup> In recent years, more experimental and theoretical evidences have been presented, which support the fact that electron transfer plays a dominant role during the CE process. Xu *et al.* designed a high temperature-resistant TENG, which realized the real-time quantitative measurement of surface charges and revealed the relationship between the

charge density and time at different temperatures.<sup>14,15</sup> The results confirmed that the electron transfer was responsible for the CE between different solid materials, and an "electron cloud-potential well" model, which was named as the "Wang transition" model, was proposed. The effect of the surface curvature on the CE suggested that the charge transfer was also dominated by electron transfer between two identical materials.<sup>16</sup> Lin *et al.* used ultraviolet light to excite the surface charges on the insulator surface, which was generated by rubbing with an atomic force microscopy (AFM) tip.<sup>17</sup> It was

Received: May 19, 2021

Accepted: July 14, 2021

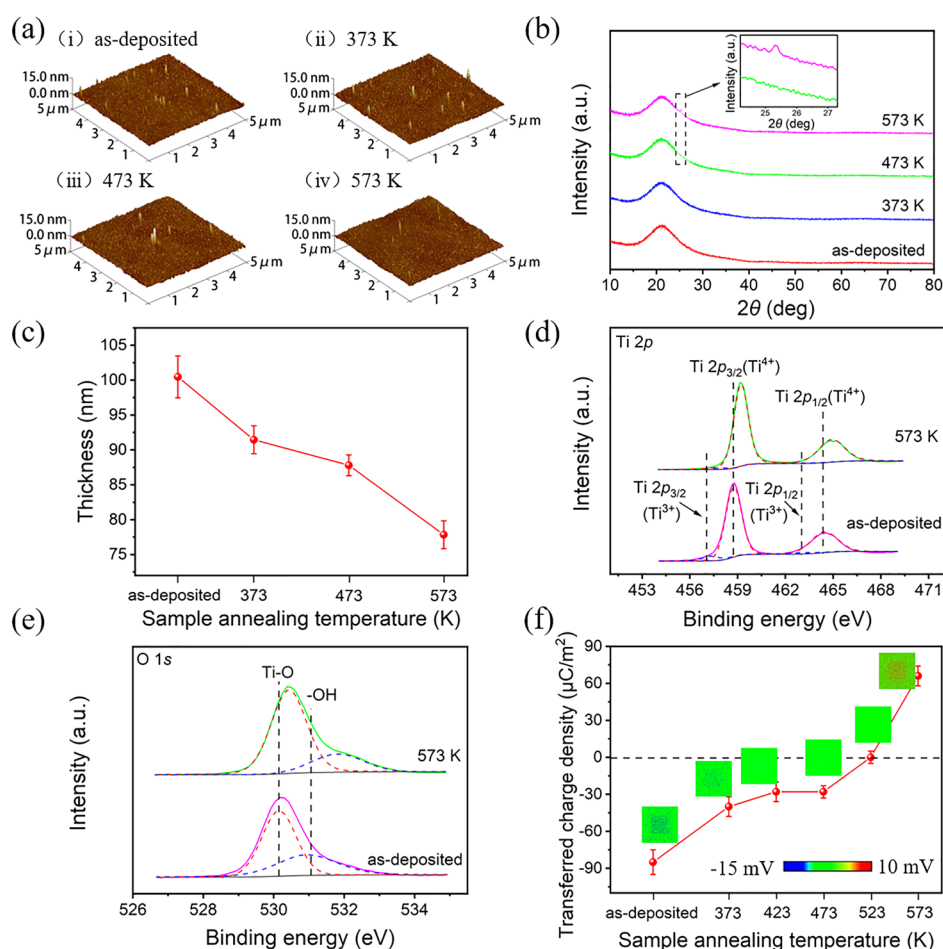


**Figure 1.** Property change and triboelectric charge evolution of TiO<sub>2-x</sub> films with 20 sccm O<sub>2</sub> deposition. (a) Surface topographies of the films. (b) XRD results of the films. (c) Thickness of the films. XPS spectra of (d) Ti 2p and (e) O 1s on the films. (f) Triboelectric charge densities under the room temperature on the films before and after the samples being annealed at different temperatures in air.

found that the triboelectric charges could be emitted from the surface by light irradiation, which further suggested that the triboelectric charges on the surface were electrons. In addition, by applying tension or pressure on the surface, Sow *et al.* found that both the magnitude and polarity of transferred charges on a poly(tetrafluoroethylene) (PTFE) surface could be modified.<sup>18</sup> Li *et al.* used low-energy helium ion irradiation to change the surface molecular structure of materials through nuclear energy loss, which improved the triboelectric properties of Kapton.<sup>19</sup> These studies suggest that the surface properties of materials are crucial to electrification.

Annealing is a common post-treatment method used to optimize the properties of materials, especially films. For example, the stoichiometric ratio of the films can be changed by annealing in different atmospheres.<sup>20</sup> Moreover, annealing at different temperatures enables the valence states of elements in the films to be controllable.<sup>21</sup> In particular, annealing can only change the properties of the very shallow surface without changing the overall characteristics of the films.<sup>22</sup> Therefore, if we altered the molar ratio or the valence state of elements on the film surface through different annealing methods, it would be very interesting to explore the specific correlations between these changes and the CE.

In this study, different kinds of substoichiometric oxide films, including TiO<sub>2-x</sub>, Al<sub>2</sub>O<sub>3-x</sub>, Ta<sub>2</sub>O<sub>5-x</sub>, and Cr<sub>2</sub>O<sub>3-x</sub>, were deposited by an electron beam evaporation method and

annealed at different temperatures, the CE of which was studied. The surface morphologies, microstructures, thickness, surface composition, and element valence states of the films were characterized and analyzed, and the relationship between the triboelectric characteristics of the films and annealing temperatures was explored by Kelvin probe force microscopy (KPFM) under the room temperature. Moreover, TiO<sub>2-x</sub>-based identical material TENGs (IM-TENGs) were developed and prepared by a simple annealing treatment, which realized the effective control of the current direction. Further, a surface state model of the CE between metal and dielectric annealed at different temperatures was proposed, and the internal relationship between the surface states and the CE was deeply discussed.

## 2. RESULTS

Figure 1a shows the surface topographies of TiO<sub>2-x</sub> films deposited at an oxygen flow rate of 20 sccm and annealed at different temperatures for 1 h. It can be found that the surface roughness of the films decreases after annealing, and the root mean square (RMS) roughness decreases gradually from 1.15 to 0.83 nm. The X-ray diffractometer (XRD) patterns in Figure 1b show that the as-deposited film is amorphous and has no crystalline phase transition after annealing at 473 K. However, a weak diffraction peak at  $2\theta = 25.3^\circ$  corresponding to the anatase (101) plane is observed after 573 K annealing. It

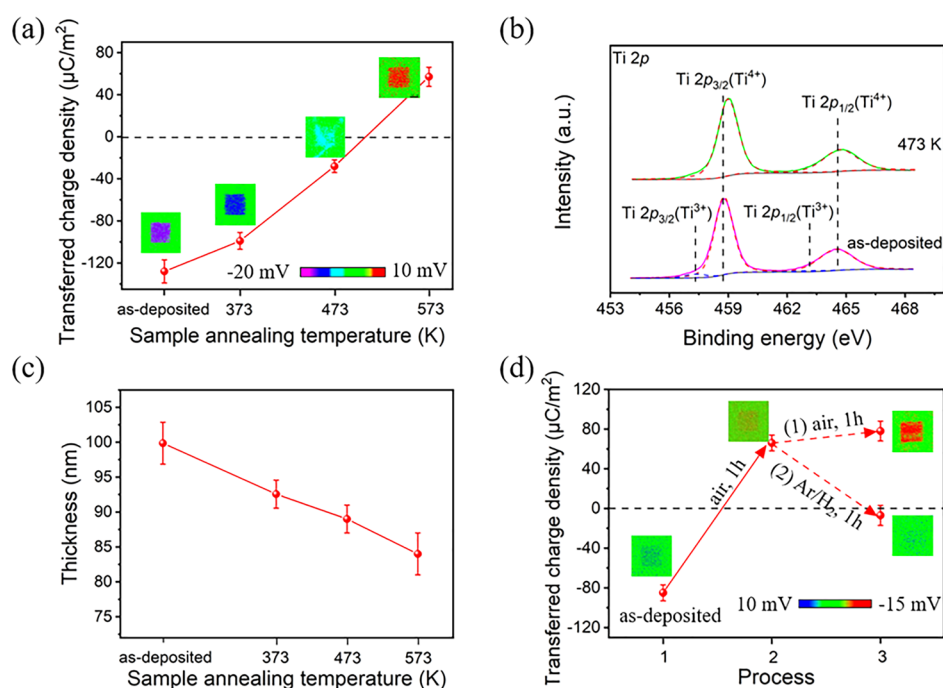


**Figure 2.** Triboelectric charge evolution of TiO<sub>2-x</sub> films with 80 sccm O<sub>2</sub> deposition. (a) Triboelectric charge densities under the room temperature on the films before and after the samples being annealed at different temperatures in air. (b) XPS spectra of Ti 2p on the films. (c) Thickness of the films. (d) Triboelectric charge densities under the room temperature on the films after treated under different annealing conditions.

indicates that the amorphous TiO<sub>2-x</sub> is transformed into anatase phase. In Figure S1, after annealing at 573 K for 4.5 h, two diffraction peaks appear, which are the corresponding anatase (101) plane of  $2\theta = 25.3^\circ$  and the anatase (200) plane of  $2\theta = 48.1^\circ$ .<sup>23,24</sup> Figure 1c shows that the thickness of the films decreases with the increase of annealing temperature. Figure 1d,e shows the X-ray photoelectron spectroscopy (XPS) results of Ti 2p and O 1s on the films, respectively. It can be seen that Ti 2p presents a representative bimodal structure, and the binding energies of two Ti 2p<sub>3/2</sub> after peak fitting are 457.3 and 458.7 eV, respectively. In Figure 1e, Ti–O at 530.2 eV and –OH at 530.9 eV are observed after the peak split of O 1s. With the increase of annealing temperature, the proportion of Ti–O gradually increases from 62.2 to 77.2%. Here, according to the energy difference,  $\Delta(\text{O–Ti}) = \text{BE}(\text{O } 1s) - \text{BE}(\text{Ti } 2p_{3/2}) = 72.9 \text{ eV}$ , the peak of the binding energy at 457.3 eV is Ti<sup>3+</sup>. The energy difference  $\Delta(\text{O–Ti}) = \text{BE}(\text{O } 1s) - \text{BE}(\text{Ti } 2p_{3/2}) = 71.5 \text{ eV}$  suggests that the peak of the binding energy at 458.7 eV is Ti<sup>4+</sup>.<sup>25,26</sup> After annealing at 573 K, the Ti<sup>4+</sup> content increases from 91.3 to 98.3%, while the Ti<sup>3+</sup> content decreases to 1.7%, which indicates further oxidation of the film by annealing. The triboelectric charges on the film surface generated by contact with a Pt coated tip are measured using peak force tapping mode and KPFM mode. As shown in Figure 1f, the surface potential on the films before and after the samples annealing at different temperatures is –12, –5.6, –4, –4, 0, and 9.3 mV, respectively. The surface charge density is calculated according to the following equation<sup>27</sup>

$$\sigma = \frac{\Delta V \epsilon_0 \epsilon_{\text{TiO}_2}}{t_{\text{TiO}_2}} \quad (1)$$

where  $\epsilon_0$  is the vacuum dielectric constant, and  $\epsilon_{\text{TiO}_2}$  and  $t_{\text{TiO}_2}$  are the relative dielectric constant and thickness of TiO<sub>2</sub>,

respectively. The calculated surface charge densities are –85, –40, –28, 0, and 66 μC/m<sup>2</sup>, respectively, which means that the charge density decreases gradually with the increase of the sample annealing temperature and charge direction reverses from original negative to positive. In addition, Figure S2 shows that the triboelectric charge densities on TiO<sub>2-x</sub> films annealed at 573 K at different times do not change significantly, indicating that the sample annealing temperature rather than the annealing time plays a dominant role in the CE.

Figure 2a shows the triboelectric charge densities on TiO<sub>2-x</sub> films deposited at an oxygen flow rate of 80 sccm and annealed at different temperatures, which are –128, –99, –28, and 57 μC/m<sup>2</sup>, respectively. With the increase of the sample annealing temperature, the polarity of transferred charges on the films changes from negative to positive, which is consistent with the results in Figure 1f. Figures 2b and S3 show the XPS spectra of Ti 2p and O 1s on the films, respectively. It can be seen that the Ti element mainly exists as Ti<sup>4+</sup> before annealing, with only a small amount of Ti<sup>3+</sup>. After annealing at 473 K, Ti<sup>3+</sup> is completely oxidized to Ti<sup>4+</sup>. In addition, Table S1 shows the O/Ti molar ratio estimated from the XPS peak areas with their relative sensitivity factors, which increases to 2.01 after annealing at 473 K, indicating that the oxygen vacancies have been basically eliminated and the main composition of the film is TiO<sub>2</sub>. Figure 2c shows that the thickness of the films also decreases gradually with the increase of the annealing temperature. In order to verify whether the change of transferred charge polarity on TiO<sub>2-x</sub> films is really caused by the reduction of oxygen vacancies, we optimized the annealing methods, as shown in Figure 2d. The initial transferred charge density on the as-deposited film is –85 μC/m<sup>2</sup>. After annealed in air at 573 K for 1 h, the transferred charge density rises to 66 μC/m<sup>2</sup>. After annealing again in air at 573 K for 1 h (route 1), the transferred charge density rises

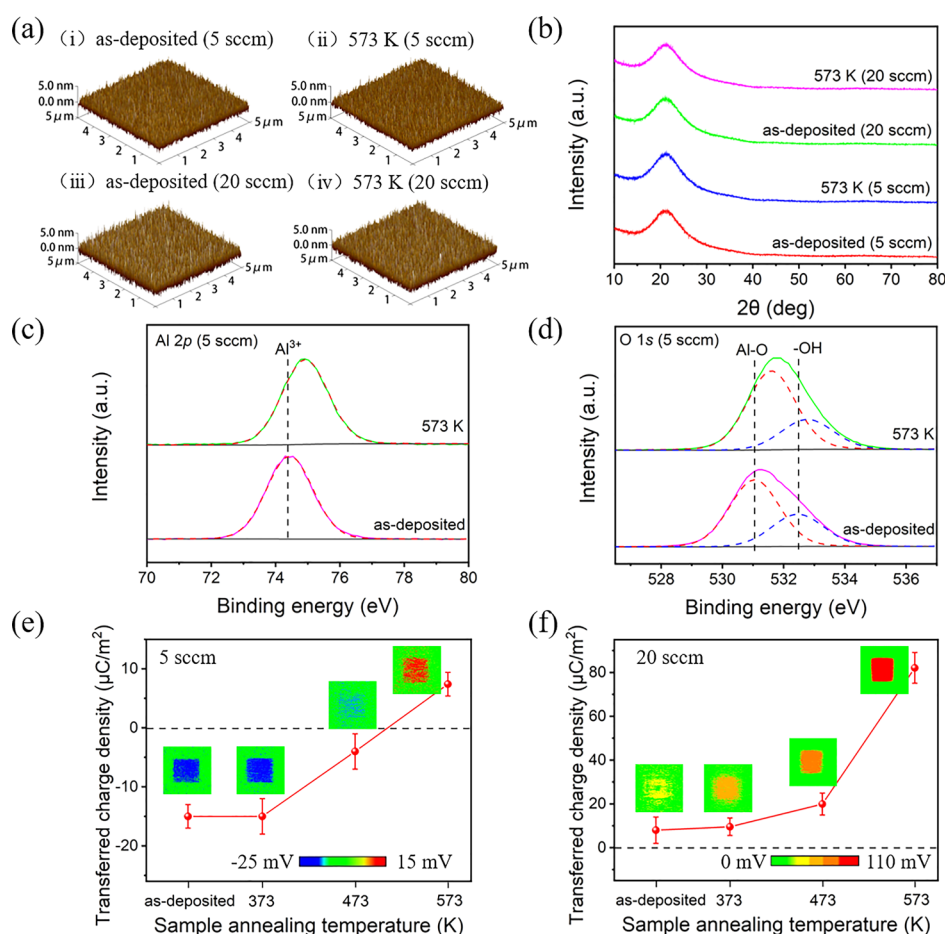


**Figure 3.** Property change and triboelectric charge evolution of  $\text{Al}_2\text{O}_{3-x}$  films. (a) Surface topographies of the films. (b) XRD results of the films. XPS spectra of (c) Al 2p and (d) O 1s on the films surface. (e) Triboelectric charge densities under the room temperature on the films with 5 sccm  $\text{O}_2$  deposition. (f) Triboelectric charge densities under the room temperature on the films with 20 sccm  $\text{O}_2$  deposition.

slightly to  $78 \mu\text{C}/\text{m}^2$ , which is consistent with the results in Figure S2. Interestingly, if the film after annealing at 573 K for 1 h in air is placed in Ar (5%  $\text{H}_2$ ) and annealed again at 573 K for 1 h (route 2), it is found that the transferred charge density turns into  $-7 \mu\text{C}/\text{m}^2$ . It indicates that the polarity of the triboelectric charges starts to change from positive to negative. These results further verify the effects of oxygen vacancy on the CE, that is, annealing in oxidizing atmosphere reduces oxygen vacancies, and the films become more likely to be positively charged, while annealing in reducing atmosphere increases oxygen vacancies, so the films become more likely to be negatively charged.

Two kinds of  $\text{Al}_2\text{O}_{3-x}$  films were deposited at oxygen flow rates of 5 and 20 sccm and annealed at different temperatures, respectively. Figure 3a shows the surface topographies of the films before and after annealing, in which the RMS roughness of the films with 5 sccm  $\text{O}_2$  deposition decreases from 0.89 to 0.84 nm, and that of the films with 20 sccm  $\text{O}_2$  deposition decreases from 1.15 to 1.08 nm. Figure 3b shows that even after 573 K annealing, both two kinds of films are still amorphous. Figure 3c,d shows the XPS spectra of Al 2p and O 1s on the films with 5 sccm  $\text{O}_2$  deposition, respectively. It can be seen that Al 2p is perfectly fitted by a peak at 74.4 eV, which indicates that the Al element in the films is  $\text{Al}^{3+}$ .<sup>28,29</sup> In addition, Al-O at 531.1 eV and -OH at 532.5 eV are observed after the peak split of O 1s, respectively.<sup>30</sup> After annealing at 573 K, the Al-O content increases from 66.6 to

72.0%. Table S2 shows that the O/Al molar ratio increases from 1.21 to 1.38 after annealing. For the films prepared with 20 sccm  $\text{O}_2$  deposition, the same trend is also observed, but the O/Al molar ratio rises to 1.50 after annealing, indicating that the composition is close to the ideal stoichiometric ratio. Figure 3e shows that the triboelectric charge densities on  $\text{Al}_2\text{O}_{3-x}$  films with 5 sccm  $\text{O}_2$  deposition before and after annealing at different temperatures are  $-15$ ,  $-15$ ,  $-4$ , and  $7.4 \mu\text{C}/\text{m}^2$ , respectively. Here, the variation of triboelectric properties of  $\text{Al}_2\text{O}_{3-x}$  films is consistent with that of  $\text{TiO}_{2-x}$  films, both of which gradually change from negative to positive with the increase of the sample annealing temperature. Interestingly, Figure 3f shows that the triboelectric charge densities on  $\text{Al}_2\text{O}_{3-x}$  films with 20 sccm  $\text{O}_2$  deposition before and after annealing at different temperatures are 8, 10, 20, and  $82 \mu\text{C}/\text{m}^2$ , respectively. It indicates that it is possible to control the initial triboelectric properties of the films by varying the oxygen supply in the deposition process. In addition, although the triboelectric charge on the as-deposited film with 20 sccm oxygen deposition is positive, it becomes more and more positive with the increase of the sample annealing temperature.

Figure 4a shows the XRD patterns of  $\text{Ta}_2\text{O}_{5-x}$  films before and after annealing. It can be seen that after annealing at 573 K, the film is still amorphous and no phase transition has been found. Figure S4 shows that with the increase of annealing temperature, the RMS roughness of the films gradually decreases from 1.01 to 0.93 nm. Figure 4b shows that Ta 4f

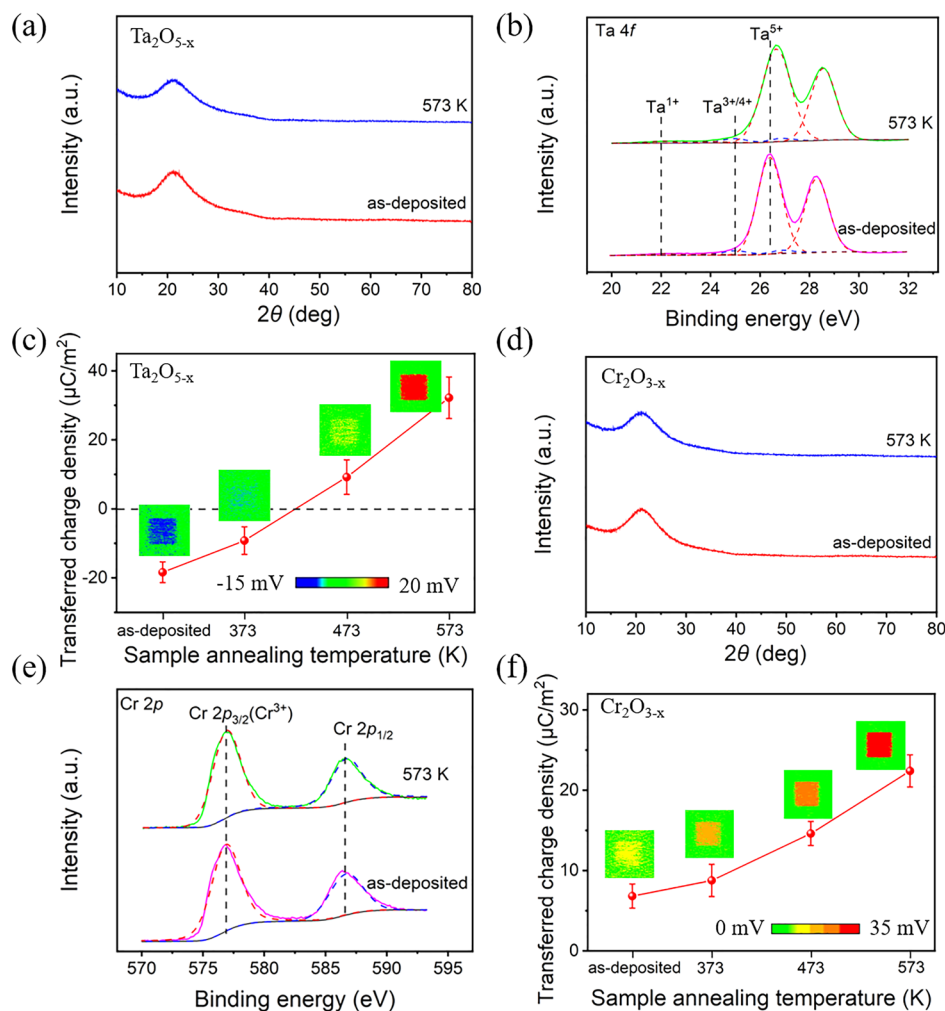


**Figure 4.** Property change and triboelectric charge evolution of  $\text{Ta}_2\text{O}_{5-x}$  films and  $\text{Cr}_2\text{O}_{3-x}$  films. (a) XRD results of the as-deposited and annealing  $\text{Ta}_2\text{O}_{5-x}$  films. (b) XPS spectra of Ta 4f on  $\text{Ta}_2\text{O}_{5-x}$  films before and after annealing. (c) Triboelectric charge densities under the room temperature on  $\text{Ta}_2\text{O}_{5-x}$  films. (d) XRD results of  $\text{Cr}_2\text{O}_{3-x}$  films before and after annealing. (e) XPS spectra of Cr 2p on  $\text{Cr}_2\text{O}_{3-x}$  films. (f) Triboelectric charge densities under the room temperature on  $\text{Cr}_2\text{O}_{3-x}$  films.

is a representative bimodal structure, and the binding energies of Ta  $4f_{7/2}$  after peak fitting are 22.1, 26.4, and 25.0 eV, respectively, corresponding to  $\text{Ta}^+$ ,  $\text{Ta}^{3+/4+}$ , and  $\text{Ta}^{5+}$ .<sup>31–33</sup> After annealing, the content of  $\text{Ta}^{5+}$  increases from 91.5 to 92.7%, indicating that the film is further oxidized. Table S3 shows that the O/Ta molar ratio gradually rises from 1.87 to 2.20 with the increase of annealing temperature, that is, the higher the temperature, the less the oxygen vacancies become. As shown in Figure 4c, the triboelectric charge densities on the films before and after annealing at different temperatures are  $-18.4$ ,  $-9.2$ ,  $9.2$ , and  $32.2 \mu\text{C}/\text{m}^2$ , respectively. Therefore, the triboelectric properties of the films also change from being likely to receive negative charges to being likely to receive positive charges. Figure 4d shows that after annealing at 573 K, the structure of  $\text{Cr}_2\text{O}_{3-x}$  film is still amorphous. In addition, the RMS roughness of the films decreases slightly from 1.11 to 1.07 nm after annealing (Figure S6). Figure 4e shows that Cr 2p is fitted by a Cr  $2p_{3/2}$  peak at 576.8 eV and Cr  $2p_{1/2}$  peak at 586.6 eV, which corresponds to the representative bimodal structure of  $\text{Cr}_2\text{O}_3$ , indicating the  $\text{Cr}^{3+}$  in the films.<sup>34,35</sup> The calculated O/Cr molar ratio rises from 0.92 to 1.06 after annealing, indicating the decreased oxygen vacancies. Figure 4f

shows that  $\text{Cr}_2\text{O}_{3-x}$  films are more likely to be positively charged with the increase of the sample annealing temperature.

As mentioned above, annealing changes the amount and even the polarity of the transferred surface charges on the films in the subsequent CE process. Therefore, we tried to adopt the annealing treatment to prepare the  $\text{TiO}_{2-x}$  based IM-TENGs. As shown in Figure 5a, one contact layer of the IM-TENG is the as-deposited  $\text{TiO}_{2-x}$  film on an FTO conductive glass, and the other contact pair is the  $\text{TiO}_{2-x}$  film coated on the FTO conductive glass annealed at 573 K. In addition, the IM-TENGs with both sides of as-deposited  $\text{TiO}_{2-x}$  films and both sides of annealed  $\text{TiO}_{2-x}$  films are also prepared, respectively. Figure 5b,c shows the positive open circuit voltage ( $V_{\text{OC}}$ ) and negative short circuit transfer charge ( $Q_{\text{SC}}$ ) of the IM-TENG formed by the as-deposited film on the left side and the annealed film on the right side. It should be noted that the traditional grounded method was used to determine  $V_{\text{OC}}$  in this study, so the measured value may be slightly smaller than the actual value.<sup>36,37</sup> The results indicates that the as-deposited film is easier to receive electrons. Here, the TENG composed of a PTFE film and Cu foil is used as a reference to test the direction of current. The left PTFE is fixed, and the right Cu approaches and contacts the PTFE. The results show the

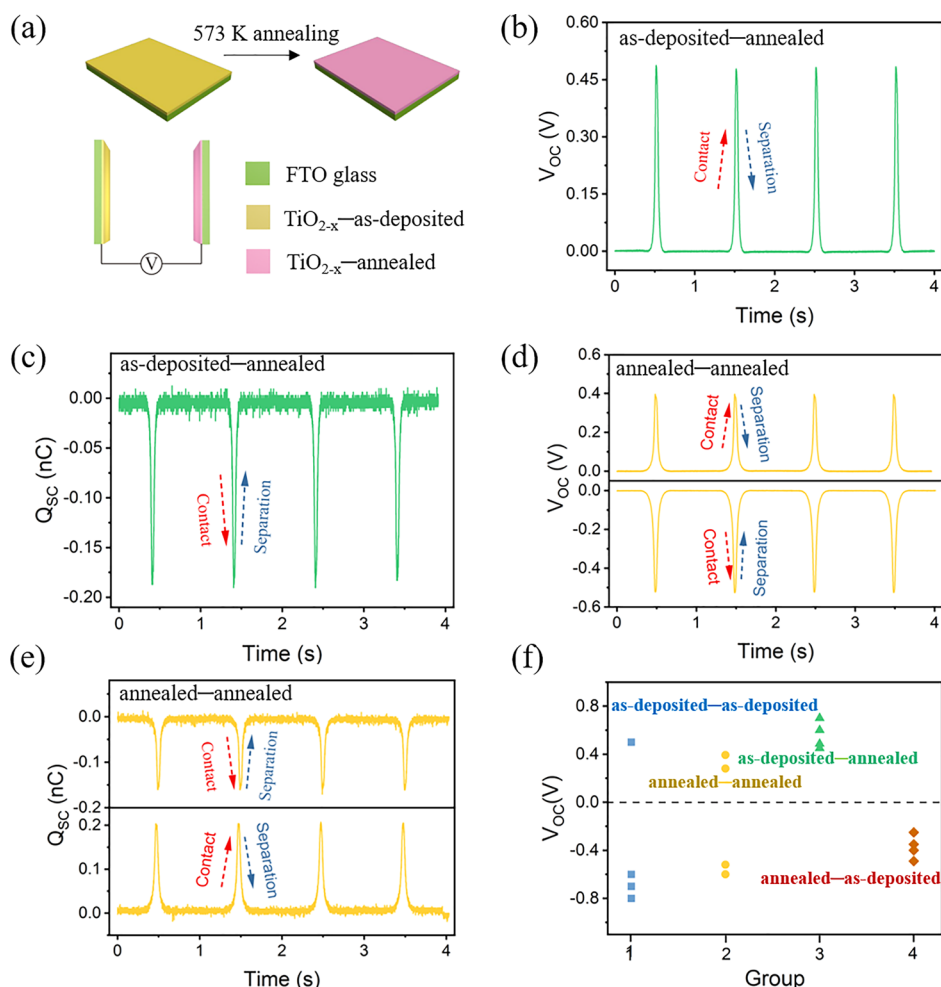


**Figure 5.** Performance of the  $\text{TiO}_{2-x}$  based IM-TENGs. (a) Schematic illustration of the IM-TENGs. (b,c) Typical  $V_{\text{OC}}$  and  $Q_{\text{SC}}$  of the IM-TENG made from the as-deposited and 573 K annealed  $\text{TiO}_{2-x}$  films. (d,e) Typical  $V_{\text{OC}}$  and  $Q_{\text{SC}}$  of the IM-TENG made from both the 573 K annealed  $\text{TiO}_{2-x}$  films. (f)  $V_{\text{OC}}$  of different groups of the IM-TENGs.

positive  $V_{\text{OC}}$  and negative  $Q_{\text{SC}}$ . Figure 5d,e shows the typical  $V_{\text{OC}}$  and  $Q_{\text{SC}}$  of the IM-TENG consisting of annealed films on both sides. The results show that the direction of electron flow is not fixed. Figure 5f shows the multiple measurement results of different groups of IM-TENGs. Here, group 1 and group 2 are the IM-TENGs with as-deposited films and annealed films on both sides, respectively. The results show that it is difficult to confirm which side is more likely to obtain electrons. Group 3 is the IM-TENGs with an as-deposited film on the left side and the annealed film on the right side. The two contact films from group 3 are exchanged in group 4. The results show that the electron flow in both group 3 and group 4 is from the annealed film to the as-deposited film, indicating that the latter is easier to capture electrons. It is consistent with the results of the as-deposited  $\text{TiO}_{2-x}$  film given in Figures 1 and 2. Moreover, it also suggests that by a simple annealing treatment, it is possible to use the identical materials to prepare the IM-TENGs which can control the current direction or the voltage output.

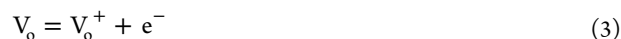
### 3. DISCUSSION

In this study, substoichiometric oxide films were deposited by electron beam evaporation and post-treated by annealing at low temperatures. Here, the overall structure of the films is not drastically changed by such annealing treatment, but slight

regulation of the stoichiometric ratio or the valence state of elements on the very shallow surface is achieved. The results show that the triboelectric charges on the films change from negative to positive gradually with the increase of the sample annealing temperature. This phenomenon is mainly due to the existence of oxygen vacancies in the films, which are reduced after annealing in the air. Here, the defect equation generated by oxygen vacancy  $V_{\text{o}}$  can be expressed as



Meanwhile, oxygen vacancy may exist in different ionization forms, and the defect equations are as follows



Therefore, the overall defect equation is as follows



According to eq 5, the oxygen vacancy eventually carries two positive charges, which tends to attract negative charges to neutralize. Therefore, the strong electron-withdrawing characteristics of oxygen vacancy are considered to be the most important reason for the change in the triboelectricity results of the films. Based on the abovementioned analysis, we

propose a surface state model to elaborate CE mechanisms of metal and dielectric annealed at different temperatures. It is assumed that the  $E_n$  of the dielectrics is higher than that occupied by electrons in the metal. Figure 6a–c schematically

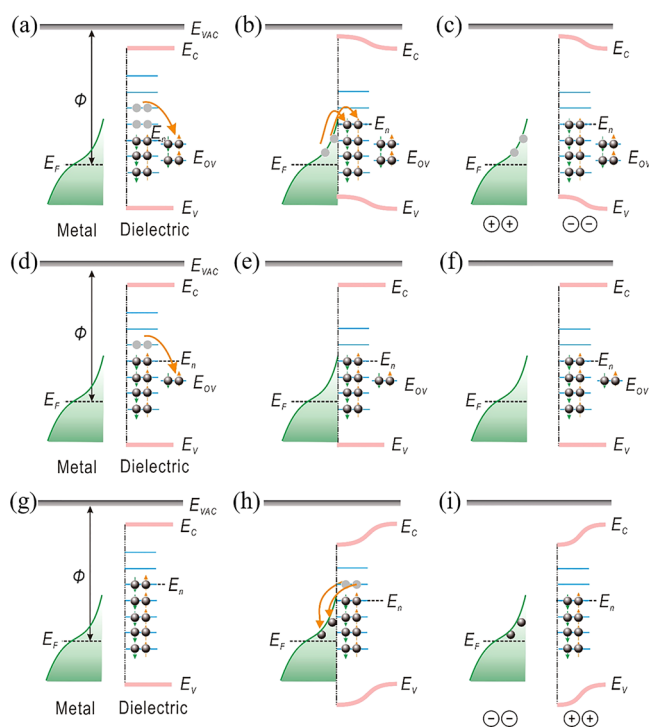


**Figure 6.** Surface states model for explaining the CE mechanisms of metal and dielectric annealed at different temperatures. (a–c) Charge transfer between metal and dielectric before annealing, (d–f) charge transfer between metal and dielectric after  $T_1$  annealing, and (g–i) charge transfer between metal and dielectric after  $T_2$  annealing.  $\Phi$ , metal work function;  $E_F$ , Fermi level;  $E_{VAC}$ , vacuum level;  $E_C$ , conduction band;  $E_n$ , neutral level of surface states;  $E_V$ , valence band;  $E_{OV}$ , level of oxygen vacancy;  $T_1$  and  $T_2$ , temperature;  $T_1 < T_2$ .

illustrates electron transfer between metal and dielectric without annealing before, during and after their contact. Here, the metal has a work function of  $\Phi$ , and its electron distribution conforms to the Fermi–Dirac distribution function. Due to the insufficient oxygen in the process of film preparation, the film contains many oxygen vacancies. The electron-withdrawing properties of oxygen vacancy may lead to the transition of electrons on the dielectric surface to the vacancy, which makes the actual occupied  $E_n$  lower than the energy level occupied by electrons in metal (Figure 6a). When the two materials are in contact, electrons in the metal will jump into the dielectric, resulting in an  $E_n$  that is identical to the highest energy level occupied by electrons in the metal (Figure 6b). When the two materials are separated, the metal is positively charged, while the dielectric is negatively charged, thereby resulting in CE (Figure 6c). Figure 6d–f schematically illustrates electron transfer between metal and dielectric before, during and after their contact after annealing at temperature  $T_1$ . Due to the elimination of some oxygen vacancies in dielectrics by annealing, only a small number of electrons are transferred from the dielectric surface to these vacancies. At this time, the energy level occupied by the electrons in the dielectric is equal to that occupied by the electrons in the metal (Figure 6d). Therefore, electron transfer does not occur when

the two materials are in contact with each other (Figure 6e). When the two materials are separated, neither the metal nor the dielectric is charged (Figure 6f). If the annealing temperature increases from  $T_1$  to  $T_2$ , the oxygen vacancies on the dielectric surface will be completely eliminated (Figure 6g). Because the  $E_n$  of the dielectric is higher than the highest energy level occupied by the electrons in the metal, the electrons in the dielectric will jump to the metal when the two materials are in contact, so that  $E_n$  is equal to the highest energy level occupied by the electrons in the metal (Figure 6h). When the two materials are separated, the dielectrics are positively charged, while the metals are negatively charged (Figure 6i). Investigation into electrification characteristics of substoichiometric oxide materials after annealing in this study is an interesting supplement to related research that looks into impacts of temperature on the CE.

#### 4. CONCLUSIONS

In conclusion, the CE of a variety of oxide films with oxygen vacancies or low cation valence states is studied. It is found that  $TiO_{2-x}$  films after annealing in air are more likely to be positively charged. This is mainly due to the repair of oxygen vacancies and the promotion of low valence  $Ti^{3+}$  to stable  $Ti^{4+}$  during annealing because the air is an oxidizing atmosphere. Likewise, when the films are annealed in  $Ar/H_2$  reducing atmosphere, they are more likely to receive negative charges. By studying the CE between  $Al_2O_{3-x}$ ,  $Ta_2O_{5-x}$ ,  $Cr_2O_{3-x}$  films and a Pt coated tip, it is further proved that the elimination of oxygen vacancies is the main reason for the films to be positively charged. Based on the abovementioned results, the IM-TENGs are designed and prepared by using  $TiO_{2-x}$  films before and after annealing. Moreover, a surface state model to elaborate CE mechanisms of metal and dielectric annealed at different temperatures is proposed. It is revealed that the oxygen vacancy changes the barrier energy of bound electrons mainly by affecting the surface states, which leads to electron transfer and CE. The study provides an interesting method to prepare the IM-TENGs which can accurately control the current direction or voltage output by using any kind of identical materials with different annealing treatment. This will provide a new direction for the application and development of the TENGs in the future.

#### 5. METHODS

**5.1. Preparation and Characterization of the Films.** Ti pellet (99.9%), Al pellet (99.999%),  $Ta_2O_5$  powder (99.99%), and Cr pellet (99.95%) were purchased from ZhongNuo Advanced Material (Beijing) Technology Co., Limited. All the substoichiometric oxide films used in this study were deposited by the electron beam evaporation method. By using Ti pellet as a coating material, two kinds of  $TiO_{2-x}$  films were deposited on high conductive Si substrates under the base pressure of  $1.5 \times 10^{-5}$  Pa when the  $O_2$  flow rate was 20 and 80 sccm, respectively. Two kinds of  $Al_2O_{3-x}$  films were deposited on high conductive Si substrates by using Al Pellet under the base pressure of  $1.5 \times 10^{-5}$  Pa when the  $O_2$  flow rate was 5 and 20 sccm, respectively.  $Ta_2O_{5-x}$  films were deposited on high conductive Si substrates by using  $Ta_2O_5$  powder under the base pressure of  $1.5 \times 10^{-5}$  Pa without oxygen supply.  $Cr_2O_{3-x}$  films were deposited on high conductive Si substrates by using Cr pellet under the base pressure of  $1.5 \times 10^{-5}$  Pa and the  $O_2$  flow rate of 20 sccm. The as-deposited films were annealed in air at 373, 473, and 573 K for 1 h, respectively. After annealing, all the samples were stored in a glovebox with nitrogen atmosphere and relative humidity less than 1%. The microstructure of the films was determined by a D8 Advance XRD. The thickness of the films was tested with a surface profiler. The chemical composition of

the films was analyzed by a thermo ESCALAB 250 X-ray photoelectron spectroscope.

**5.2. AFM Equipment.** All the experiments were performed on a commercial AFM/KPFM equipment Icon (Bruker, USA) under the room temperature. The conductive tip used here was Multi75E-G (BudgetSensors, Bulgaria; Pt-coated; tip radius: 25 nm; spring constant:  $3 \text{ N m}^{-1}$ ). In the peakforce tapping scanning, the scan size was set to  $5 \mu\text{m}$  and the scan rate was 1 Hz. The peakforce was about 2 nN when the tip was scanning the oxide films. The triboelectric charges were detected in the KPFM mode, while the tapping amplitude was set to 350 mV, the lift height was 50 nm, and the scan size was  $10 \mu\text{m}$ . All the tests were conducted in a nitrogen atmosphere and relative humidity less than 1%.

**5.3. Fabrication and Measurement of the IM-TENGs.** FTO conductive glasses with a size of  $40 \times 30 \times 2.2 \text{ mm}$  were used as the substrates here.  $\text{TiO}_{2-x}$  films were deposited on the FTO substrates under the base pressure of  $1.5 \times 10^{-5} \text{ Pa}$  and the  $\text{O}_2$  flow rate of 40 sccm. Four kinds of IM-TENGs were prepared with  $\text{TiO}_{2-x}$  films before and after annealing. The effective area of all the IM-TENGs was  $9 \text{ cm}^2$ . The short-circuit transfer charge  $Q_{\text{SC}}$  and open-circuit voltage  $V_{\text{OC}}$  of the IM-TENGs were measured by a Keithley 6514 electrometer and collected by LabVIEW software.

## ■ ASSOCIATED CONTENT

### SI Supporting Information

The Supporting Information is available free of charge at <https://pubs.acs.org/doi/10.1021/acsami.1c09248>.

XRD pattern, triboelectric charge data, XPS spectra and results, surface topographies, and list of element content on films (PDF)

## ■ AUTHOR INFORMATION

### Corresponding Authors

**Cheng Xu** – School of Materials Science and Engineering, China University of Mining and Technology, Xuzhou 221116, China; Beijing Institute of Nanoenergy and Nanosystems, Chinese Academy of Sciences, Beijing 100083, China; [orcid.org/0000-0002-1680-0323](https://orcid.org/0000-0002-1680-0323); Email: [xucheng@cumt.edu.cn](mailto:xucheng@cumt.edu.cn)

**Zhong Lin Wang** – Beijing Institute of Nanoenergy and Nanosystems, Chinese Academy of Sciences, Beijing 100083, China; School of Materials Science and Engineering, Georgia Institute of Technology, Atlanta, Georgia 30332-0245, United States; [orcid.org/0000-0002-5530-0380](https://orcid.org/0000-0002-5530-0380); Email: [zhong.wang@mse.gatech.edu](mailto:zhong.wang@mse.gatech.edu)

### Authors

**Yongqiao Zhu** – School of Materials Science and Engineering, China University of Mining and Technology, Xuzhou 221116, China

**Shiquan Lin** – Beijing Institute of Nanoenergy and Nanosystems, Chinese Academy of Sciences, Beijing 100083, China

**Wenchao Gao** – Department of Civil Engineering, Monash University, Clayton 3800, Australia

**Miao Zhang** – School of Materials Science and Engineering, China University of Mining and Technology, Xuzhou 221116, China

**Chaogui Yang** – School of Materials Science and Engineering, China University of Mining and Technology, Xuzhou 221116, China

**Peizhong Feng** – School of Materials Science and Engineering, China University of Mining and Technology, Xuzhou 221116, China

Complete contact information is available at:

<https://pubs.acs.org/doi/10.1021/acsami.1c09248>

### Author Contributions

<sup>†</sup>Y.Z., S.L., and W.G. contributed equally to this work.

### Notes

The authors declare no competing financial interest.

## ■ ACKNOWLEDGMENTS

C.X. thanks the Fundamental Research Funds for the Central Universities (2019ZDPY05).

## ■ REFERENCES

- (1) Lowell, J. Surface States and the Contact Electrification of Polymers. *J. Phys. D: Appl. Phys.* **1977**, *10*, 65–71.
- (2) Lowell, J.; Rose-Innes, A. C. Contact Electrification. *Adv. Phys.* **1980**, *29*, 947–1023.
- (3) Hays, D. A. Contact Electrification Between Mercury and Polyethylene: Effect of Surface Oxidation. *J. Chem. Phys.* **1974**, *61*, 1455–1462.
- (4) Fan, F.-R.; Tian, Z.-Q.; Wang, Z. L. Flexible Triboelectric Generator. *Nano Energy* **2012**, *1*, 328–334.
- (5) Wang, Z. L. On Maxwell's Displacement Current for Energy and Sensors: the Origin of Nanogenerators. *Mater. Today* **2017**, *20*, 74–82.
- (6) Wang, Z. L.; Wang, A. C. On the Origin of Contact-Electrification. *Mater. Today* **2019**, *30*, 34–51.
- (7) Su, Y.; Wen, X.; Zhu, G.; Yang, J.; Chen, J.; Bai, P.; Wu, Z.; Jiang, Y.; Wang, Z. L. Hybrid Triboelectric Nanogenerator for Harvesting Water Wave Energy and As a Self-Powered Distress Signal Emitter. *Nano Energy* **2014**, *9*, 186–195.
- (8) Zhao, J.; Zhen, G.; Liu, G.; Bu, T.; Liu, W.; Fu, X.; Zhang, P.; Zhang, C.; Wang, Z. L. Remarkable Merits of Triboelectric Nanogenerator Than Electromagnetic Generator for Harvesting Small-Amplitude Mechanical Energy. *Nano Energy* **2019**, *61*, 111–118.
- (9) Shao, J.; Jiang, T.; Tang, W.; Xu, L.; Kim, T. W.; Wu, C.; Chen, X.; Chen, B.; Xiao, T.; Bai, Y.; Wang, Z. L. Studying About Applied Force and the Output Performance of Sliding-Mode Triboelectric Nanogenerators. *Nano Energy* **2018**, *48*, 292–300.
- (10) Liu, C.-y.; Bard, A. J. Electrons on Dielectrics and Contact Electrification. *Chem. Phys. Lett.* **2009**, *480*, 145–156.
- (11) McCarty, L. S.; Whitesides, G. M. Electrostatic Charging Due to Separation of Ions at Interfaces: Contact Electrification of Ionic Electrets. *Angew. Chem., Int. Ed.* **2008**, *47*, 2188–2207.
- (12) Diaz, A. F.; Wollmann, D.; Dreblow, D. Contact Electrification: Ion Transfer to Metals and Polymers. *Chem. Mater.* **1991**, *3*, 997–999.
- (13) Lowell, J. The Role of Material Transfer in Contact Electrification. *J. Phys. D: Appl. Phys.* **1977**, *10*, L233–L235.
- (14) Xu, C.; Zhang, B.; Wang, A. C.; Cai, W.; Zi, Y.; Feng, P.; Wang, Z. L. Effects of Metal Work Function and Contact Potential Difference on Electron Thermionic Emission in Contact Electrification. *Adv. Funct. Mater.* **2019**, *29*, 1903142.
- (15) Xu, C.; Wang, A. C.; Zou, H.; Zhang, B.; Zhang, C.; Zi, Y.; Pan, L.; Wang, P.; Feng, P.; Lin, Z.; Wang, Z. L. Raising the Working Temperature of a Triboelectric Nanogenerator by Quenching Down Electron Thermionic Emission in Contact-Electrification. *Adv. Mater.* **2018**, *30*, 1803968.
- (16) Xu, C.; Zhang, B. B.; Wang, A. C.; Zou, H. Y.; Liu, G. L.; Ding, W. B.; Wu, C. S.; Ma, M.; Feng, P. Z.; Lin, Z. Q.; Wang, Z. L. Contact-Electrification Between Two Identical Materials: Curvature Effect. *ACS Nano* **2019**, *13*, 2034–2041.
- (17) Lin, S.; Xu, L.; Zhu, L.; Chen, X.; Wang, Z. L. Electron Transfer in Nanoscale Contact Electrification: Photon Excitation Effect. *Adv. Mater.* **2019**, *31*, 1901418.

- (18) Sow, M.; Widenor, R.; Kumar, A.; Lee, S. W.; Lacks, D. J.; Sankaran, R. M. Strain-Induced Reversal of Charge Transfer in Contact Electrification. *Angew. Chem., Int. Ed.* **2012**, *51*, 2695–2697.
- (19) Li, S.; Fan, Y.; Chen, H.; Nie, J.; Liang, Y.; Tao, X.; Zhang, J.; Chen, X.; Fu, E.; Wang, Z. L. Manipulating the Triboelectric Surface Charge Density of Polymers by Low-Energy Helium Ion Irradiation/Implantation. *Energy Environ. Sci.* **2020**, *13*, 896–907.
- (20) Wang, S.; Zhang, B.; Zhao, C.; Li, S.; Zhang, M.; Yan, L. Valence Control of Cobalt Oxide Thin Films by Annealing Atmosphere. *Appl. Surf. Sci.* **2011**, *257*, 3358–3362.
- (21) Xu, C.; Dong, H.; Yuan, L.; He, H.; Shao, J.; Fan, Z. Investigation of Annealing Effects on the Laser-Induced Damage Threshold of Amorphous Ta<sub>2</sub>O<sub>5</sub> films. *Opt. Laser Technol.* **2009**, *41*, 258–263.
- (22) Xu, C.; Xu, L.-M.; Zhang, H.-Z.; Qiang, Y.-H.; Zhu, Y.-B.; Liu, J.-T.; Shao, J.-D. Comparative Studies on the Laser Damage Resistance of Ta<sub>2</sub>O<sub>5</sub> and Nb<sub>2</sub>O<sub>5</sub> Films Performed under Different Electron Beam Currents. *Chin. Phys. Lett.* **2011**, *28*, 064211.
- (23) Venkatachalam, N.; Palanichamy, M.; Arabindoo, B.; Murugesan, V. Alkaline Earth Metal Doped Nanoporous TiO<sub>2</sub> for Enhanced Photocatalytic Mineralisation of Bisphenol-A. *Catal. Commun.* **2007**, *8*, 1088–1093.
- (24) Ma, L.-J.; Guo, L.-J. Study of the Phase Transformation of TiO<sub>2</sub> with In-Situ XRD in Different Gas. *Spectrosc. Spectr. Anal.* **2011**, *31*, 1133–1137.
- (25) Atuchin, V. V.; Kesler, V. G.; Pervukhina, N. V.; Zhang, Z. Ti 2p and O 1s Core Levels and Chemical Bonding in Titanium-Bearing Oxides. *J. Electron Spectrosc. Relat. Phenom.* **2006**, *152*, 18–24.
- (26) Matharu, J.; Cabailh, G.; Thornton, G. Synthesis of TiO<sub>2</sub>(110) Ultra-Thin Films on W(100) and Their Reactions with H<sub>2</sub>O. *Surf. Sci.* **2013**, *616*, 198–205.
- (27) Zhou, Y. S.; Liu, Y.; Zhu, G.; Lin, Z.-H.; Pan, C.; Jing, Q.; Wang, Z. L. In Situ Quantitative Study of Nanoscale Triboelectrification and Patterning. *Nano Lett.* **2013**, *13*, 2771–2776.
- (28) Zhang, F.; Sun, G.; Zheng, L.; Liu, S.; Liu, B.; Dong, L.; Wang, L.; Zhao, W.; Liu, X.; Yan, G.; Tian, L.; Zeng, Y. Interfacial Study and Energy-Band Alignment of Annealed Al<sub>2</sub>O<sub>3</sub> Films Prepared by Atomic Layer Deposition on 4H-SiC. *J. Appl. Phys.* **2013**, *113*, 044112.
- (29) Takhar, K.; Upadhyay, B. B.; Yadav, Y. K.; Ganguly, S.; Saha, D. Al<sub>2</sub>O<sub>3</sub> Formed by Post Plasma Oxidation of Al As a Gate Dielectric for AlGaIn/GaN MIS-HEMTs. *Appl. Surf. Sci.* **2019**, *481*, 219–225.
- (30) Zhang, L.; Li, Y.; Guo, H.; Zhang, H.; Zhang, N.; Hayat, T.; Sun, Y. Decontamination of U(VI) on Graphene Oxide/Al<sub>2</sub>O<sub>3</sub> Composites Investigated by XRD, FTIR and XPS Techniques. *Environ. Pollut.* **2019**, *248*, 332–338.
- (31) Atuchin, V. V.; Grivel, J.-C.; Zhang, Z. Core Level Photoemission Spectroscopy and Chemical Bonding in Sr<sub>2</sub>Ta<sub>2</sub>O<sub>7</sub>. *Chem. Phys.* **2009**, *360*, 74–78.
- (32) Medicherla, V. R. R.; Majumder, S.; Paramanik, D.; Varma, S. Formation of Self-Organized Ta Nano-Structures by Argon Ion Sputtering of Ta Foil: XPS and AFM Study. *J. Electron Spectrosc. Relat. Phenom.* **2010**, *180*, 1–5.
- (33) Ivanov, M. V.; Perevalov, T. V.; Aliev, V. S.; Gritsenko, V. A.; Kaichev, V. V. Electronic Structure of δ-Ta<sub>2</sub>O<sub>5</sub> with Oxygen Vacancy: Ab Initio Calculations and Comparison with Experiment. *J. Appl. Phys.* **2011**, *110*, 024115.
- (34) Ikemoto, I.; Ishii, K.; Kinoshita, S.; Kuroda, H.; Alario Franco, M. A.; Thomas, J. M. X-Ray Photoelectron Spectroscopic Studies of CrO<sub>2</sub> and Some Related Chromium Compounds. *J. Solid State Chem.* **1976**, *17*, 425–430.
- (35) Escamilla, R.; Huerta, L.; Romero, M.; Verdin, E.; Durán, A. Evidence of Mixed Valence Cr<sup>+3</sup>/Cr<sup>+4</sup> in Y<sub>1-x</sub>Ca<sub>x</sub>CrO<sub>3</sub> Polycrystalline Ceramics by X-Ray Photoelectron Spectroscopy. *J. Mater. Sci.* **2017**, *52*, 2889–2894.
- (36) Zhang, W.; Gu, G.; Qin, H.; Li, S.; Shang, W.; Wang, T.; Zhang, B.; Cui, P.; Guo, J.; Yang, F.; Cheng, G.; Du, Z. Measuring the Actual Voltage of a Triboelectric Nanogenerator Using the Non-grounded Method. *Nano Energy* **2020**, *77*, 105108.
- (37) Zhang, W.; Gu, G.; Shang, W.; Luo, H.; Wang, T.; Zhang, B.; Cui, P.; Guo, J.; Yang, F.; Cheng, G.; Du, Z. A General Charge Compensation Strategy for Calibrating the Voltage of a Triboelectric Nanogenerator Measured by a Capacitive Circuit. *Nano Energy* **2021**, *86*, 106056.